Quantifying mode-resolved coherence in phonon transport in GaN/AlN superlattices

Li-Mu Wang, Hong-Ao Yang, and Bing-Yang Cao*

Key Laboratory for Thermal Science and Power Engineering of Ministry of Education, Department of Engineering Mechanics, Tsinghua University, Beijing 100084, China

(Received 30 November 2025; revised 4 February 2026; accepted 17 February 2026; published 11 March 2026)

Understanding and engineering phonon transport in GaN/AlN superlattices (SLs) is critical for the thermal management of GaN high-electron-mobility transistors (HEMTs). While most studies suggest that interfacial roughness reduces the thermal conductivity of SLs, a few have reported its unexpected enhancement, yet the underlying mechanism, particularly concerning phonon coherence, remains elusive. In this study, we address this gap by developing ametric—the concentration degree of energy (CDE) in k-space—to directly quantify the degree of phonon coherence from atomic displacements obtained through lattice dynamics. Our simulations reveal that interfacial roughness can enhance the thermal conductivity of SLs, provided that the inherent periodicity of the SL is not disrupted. A mode-resolved coherence analysis based on the CDE metric reveals that while increased roughness leads to a rise in incoherent modes, it simultaneously enables more modes to propagate. Meanwhile, the preservation of periodicity is the decisive factor that significantly enhances phonon coherence. This insight successfully explains why SLs with moderate, periodicity-preserving roughness can achieve superior phonon coherence and higher thermal conductivity than ideal SLs. The coherence analysis framework is applicable to general SL systems.

DOI: 10.1103/q6d9-mqs6

I. INTRODUCTION

GaN-based high electron mobility transistors (HEMTs) have proven to be highly suitable for the fabrication of power and radio frequency devices due to the high saturation velocity of carriers, high breakdown field strength, and strong radiation resistance [1–5]. GaN/AlN superlattices (SLs), as a type of artificial periodic nanostructure [6], have been applied in the design of GaN HEMTs as a transition layer between the channel layer and the substrate, in order to improve the electrical performance of the channel layer [7–9]. Since GaN HEMTs generate significant heat during operation [10–12], it is crucial to facilitate heat dissipation through the GaN/AlN SL, which involves modulating the thermal conductivity of the SL. For semiconductor SLs where heat transport is dominated by phonons, this demands a profound understanding of phonon transport.

It is generally believed that SLs with atomically sharp interfaces can achieve high cross-plane thermal conductivity [13–15], for thermal transport is dominated by coherent phonons that traverse multiple interfaces without losing their phase information [16–19]. On the other hand, nonideal factors such as impurities [19,20], dislocations [21,22], and aperiodicity in layer thickness [23–25] are considered to induce incoherent phonon scatterings, thereby impeding phonon transport and reducing the thermal conductivity of SLs. Beyond the factors discussed above, the effect of interfacial roughness is the most intriguing and contentious. The prevailing view holds that roughness destroys phonon coherence and therefore lowers thermal conductivity [14,26–28], yet a few studies on Si/Ge [29,30] and GaAs/AlAs [31] SLs report that interfacial roughness can lead to higher phonon transmittance and thermal conductivity, pointing to a promising route for SL thermal management. Unfortunately, these studies have not elucidated in detail how interfacial roughness influences the coherence of different phonon modes to achieve superior thermal transport, limiting the implementation of roughness engineering across diverse SL systems.

Considerable effort has been devoted to assessing the coherence of phonon modes so far. Early criteria for identifying phonon transport as coherent include: (1) The period length of the SL is less than the phonon inelastic scattering mean free path (MFP) [32,33] or coherence length [34,35]; and (2) for rough-interface superlattices, the roughness is less than the phonon wavelength [36]. In addition, Luckyanova *et al*. proposed that the frequency range of coherent phonons can be identified based on the transmission spectra [14]. These aforementioned qualitative criteria or methods have been adopted in numerous studies to qualitatively analyze phonon coherence in SLs, yet they fail in quantitatively and precisely examining real scenarios in which phonons may exist in an intermediate state between coherence and incoherence [18,23,29]. To resolve the puzzle of thermal transport in rough-interface SLs, it is imperative to develop a metric that quantifies the degree of coherence in phonon transport.

In recent years, two representative approaches capable of investigating phonon transport behavior through direct calculation of atomic displacements—lattice dynamics (LD) [37–42] and wave packet simulations based on molecular dynamics (MD) [43–45]—have shed new light on this issue. For SL systems, wave packet simulations can capture

*Contact author: caoby@tsinghua.edu.cn

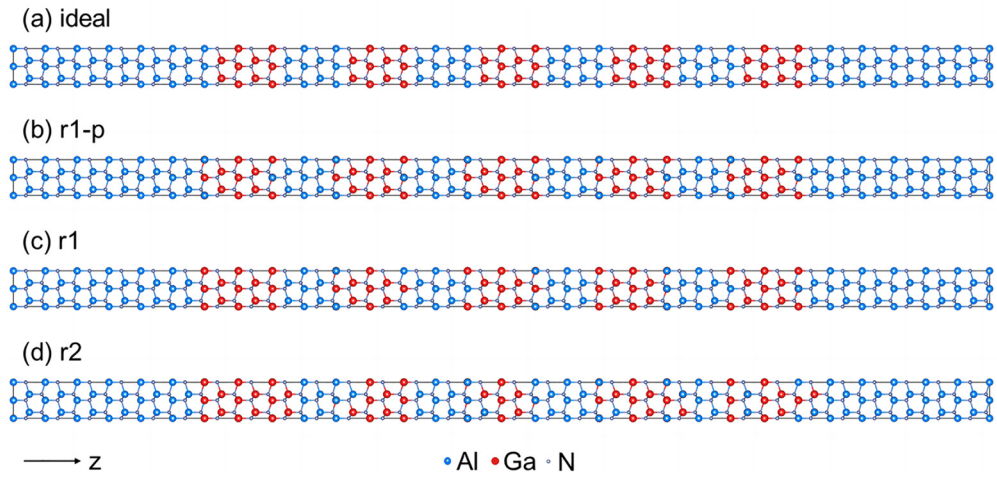

FIG. 1. Schematic of the unit cells of four types of SLs with different interface structures. (a) 'ideal': SL with atomically smooth interfaces. (b) 'r1-p': periodicity maintained SL with interfacial roughness of 1 ML. (c) 'r1': periodicity disrupted SL with interfacial roughness of 1 ML. (d) 'r2': periodicity disrupted SL with interfacial roughness of 2 ML. The actual SL models used in our study have more periods.

both coherent transport and incoherent scattering phenomena, but they are typically limited to calculating phonons with near-normal incidence [46,47]. Lattice dynamics, on the other hand, demonstrates the capability to handle phonons with large-angle incidence [39] and perform mode-resolved calculations [41]. LD possesses inherent advantages for investigating the coherent properties of phonons, while its limitation lies in the difficulty of handling anharmonic scattering. However, for rough-interface SLs, diffuse scattering at interfaces constitutes the dominant incoherent transport mechanism [19,28,48], and the existing LD methods are well suited to address this kind of scattering phenomenon [41,49].

In this study, we develop a coherence analysis framework based on LD calculations. From the atomic displacements in the SL obtained through LD, we extract a mode-resolved metric for quantifying phonon coherence—the concentration degree of energy (CDE) in k-space. To achieve a high-precision solution of atomic displacements, we trained a machine learning interatomic potential based on the MACE architecture [50]. Using the proposed metric, we conduct a comprehensive investigation into the effects of frequency, incident angle, and interfacial roughness on phonon coherence in GaN/AlN SLs, and successfully elucidate the underlying reasons and specific conditions under which interfacial roughness enhances the thermal conductivity of these SLs. The coherence analysis framework we developed can be well applied to SLs composed of other material systems.

II. METHODOLOGY

A. Superlattice structures

Since both AlN and GaN crystals are wurtzite structure, the GaN/AlN superlattice structure can be simply constructed by periodically alternating the stacking of the two component materials along the c axis. To investigate the effects of interfacial roughness, four types of SLs with different interface structures are modeled, with the schematic of their unit cells shown in Fig. 1. The first type has atomically smooth interfaces, serving as a benchmark for this study, denoted as 'ideal'. The other three types are SLs with rough interfaces. The roughness is introduced by randomly swapping the Al and Ga atoms on either side of the interface with a probability of 50%, and the number following the letter 'r' denotes the magnitude of the roughness, that is, how many monolayers (ML) near the interface are involved during the swapping process. If atoms of the same position in the local environment of each interface are swapped, the resulting SL will maintain its structural periodicity, denoted as 'p'. Otherwise, the completely random swapping of atoms near the interfaces will disrupt the periodicity of the SL. We denote the cross-plane direction of the SL as z-direction, and set the center point of the model at $z = 0$.

It is clear that the degree of structural disorder of the four types of SLs has the following size relationship: ideal $<$ r1-p $<$ r1 $<$ r2. The dimensions of these SL models in the x- and y-directions were set to 2 unit cells (UC). During the actual calculation process, periodic boundary conditions are applied to these two directions. To investigate the effect of total and period length on thermal transport, the total length of the SL models is set to 40 UC and 80 UC, while the period length is set to 2 UC, 4 UC, 6 UC, and 8 UC. We set the parameters in this way for the following two considerations: (1) The layer thickness is much shorter than the phonon MFP in bulk AlN and GaN at room temperature [51,52] so that interface scattering is the dominant mechanism for incoherent transport; and (2) the number of layers is greater than 10 to produce a significant coherent transport effect.

As shown in Fig. 1, all the SLs are extended by a certain length of bulk material on both the left and right sides for phonon properties calculation with LD. The left and right materials are both set to AlN to eliminate the effect of the mismatch of phonon dispersion on the thermal transport. It is worth noting that due to the existence of evanescent phonon modes, the length of the bulk material in z-direction cannot be too small, otherwise the thermal conductance obtained by LD will become unreliable [41]. We have performed a convergence test on the thermal conductance with respect to the length of the bulk material, and set this length for all

the calculations to 20 UC based on the result of the test (see Supplemental Material, Fig. S1 [53]).

B. Machine learning interatomic potential

To evaluate the interatomic interactions within GaN/AlN superlattice structures, we employ the recently developed MACE machine learning potential [50]. Initial atomic configurations were generated using the general MACE-MP potential function [54], which was pretrained on the Materials Project dataset.

Regarding dataset construction, the dataset specifically comprises three primary components: pure AlN crystals, pure GaN crystals, and GaN/AlN interfaces. To illustrate the dataset construction process using AlN crystals as an example, the primitive AlN crystal was first expanded into a supercell using the transformation matrix [(5, 0, 0), (3, 6, 0), (0, 0, 3)]. This resulted in a nearly cubic supercell with approximate dimensions of 16 Å × 16 Å × 15 Å, containing 360 atoms. Subsequently, the lattice constants were scaled by factors ranging from 0.96 to 1.04 in 0.01 increments. This procedure aimed to generate datasets under various strain conditions, thereby enhancing the stability of the potential function, resulting in a total of nine distinct strain conditions. Following this, for each strain state, molecular dynamics (MD) simulations of 10 000 steps were performed, driven by the MACE-MP potential. A Langevin thermostat was employed to maintain the temperature at 1000 K during these simulations. Subsequently, 20 representative configurations were selected from these 10 000-step MD trajectories using the random structure search (RSS) method [55]. Finally, these 180 structures were subjected to density functional theory (DFT) calculations to relabel their atomic forces and energies. An analogous procedure was applied to construct datasets for pure GaN crystals and GaN/AlN interfaces, respectively. This yielded a total of 540 structures.

All DFT calculations were performed using the Vienna *Ab initio* Simulation Package (VASP) [56]. The projector augmented wave (PAW) [57] method was employed in conjunction with the Perdew-Burke-Ernzerhof (PBE) [58] exchange-correlation functional. A consistent plane-wave energy cutoff of 600 eV and an electronic energy convergence criterion of 1×10^{-6} eV were utilized. Brillouin zone sampling was restricted to the Gamma point.

For the MACE potential training, the entire dataset was partitioned into an 80% training set, a 10% validation set, and a 10% test set. A hidden representation with dimensions of 64+64 was employed. The model was trained for 200 epochs. The final root mean square error (RMSE) achieved was 1.9 meV/atom for energy and 11 meV/Å for forces. Furthermore, we have made a comparison of the phonon dispersion calculated by DFT and MACE potential to validate the effectiveness of the MACE potential (see Supplemental Material, Note B [53]).

C. Lattice dynamics

The basic process of LD is as follows. The first step is to define the computational region and relax the structure so that all atoms reside at their equilibrium positions. The structure is divided into three regions: the left, the center, and the right. The left and right regions are uniform bulk materials (AlN for this case), which are used for calculating phonon frequencies and eigenvectors. The central region comprises the material system under investigation, specifically the GaN/AlN superlattice in this case. The structure relaxation is conducted using the L-BFGS algorithm with the MACE interatomic potential.

The next step is to solve for the phonon properties of the left and right regions. We first calculate the second-order force constants of the system using the MACE interatomic potential. Based on the harmonic approximation, the dynamic equations of the atoms in the system are then established as

$$-\sum_{l'b'\alpha'} \Phi_{lb\alpha,l'b'\alpha'} u_{l'b'\alpha'} = m_b \frac{d^2 u_{lb\alpha}}{dt^2}, \tag{1}$$

where $\Phi_{lb\alpha,l'b'\alpha'}$ represents the second-order force constant matrix between the two atoms denoted by lb and $l'b'$ (where l stands for the l-th unit cell and b stands for the b-th atom in this cell), α is the Cartesian index, $u_{lb\alpha}$ is the atomic displacement from the equilibrium position, and m_b is the mass of the atom. In the left and right crystalline structures, the solution of Eq. (1) should have the form of a Bloch wave [59],

$$u_{lb\alpha}(t) = \frac{1}{\sqrt{N_c}} \xi_{b\alpha} \exp\left[i(\mathbf{k}\cdot\mathbf{R}_{lb} - \omega(\mathbf{k})t)\right], \tag{2}$$

where k and $\omega(\mathbf{k})$ are the phonon wave vector and frequency, $\mathbf{R}_{lb}$ is the location of the atom, N_c is the number of unit cells in the system, and ξ is the phonon eigenvector. For the wurtzite AlN, a unit cell contains four atoms, each atom having three degrees of freedom in space, thus the eigenvector ξ is 12-dimensional. By substituting Eq. (2) into Eq. (1) and introducing the dynamical matrix as

$$D_{b\alpha,b'\alpha'}(\mathbf{k}) = \frac{1}{\sqrt{m_b m_{b'}}} \sum_{l'} \Phi_{0b\alpha,l'b'\alpha'} \exp[i\mathbf{k}\cdot(\mathbf{R}_{l'b'} - \mathbf{R}_{0b})], \tag{3}$$

we can establish the eigenvalue problem as

$$\sum_{b'\alpha'} D_{b\alpha,b'\alpha'}(\mathbf{k}) \xi_{b'\alpha'} = \omega^2(\mathbf{k}) \xi_{b\alpha}. \tag{4}$$

The solution of the Eq. (4) yields the dispersion relation $\omega(\mathbf{k})$. Given an incident phonon mode (denoted as I), the reflection and transmission modes (denoted as R_j and T_p, respectively) share the same ω with the incident mode, and the wave vectors $\mathbf{k}_{R_j}$ and $\mathbf{k}_{T_p}$ can be determined based on the principles in Ref. [41]. In our simulations, the incident phonons are initialized with unit amplitude. The superposition of the R_j modes with amplitude A_{R_j} and the incident mode constitutes the atomic displacements of the left region, while the superposition of the T_p modes with amplitude A_{T_p} constitutes the atomic displacements of the right region. Hence, the atomic displacements of the left, central, and right regions can be written as

$$\begin{aligned} u_{\mathrm{L},lb\alpha}(t) &= \xi_{I,b\alpha} \exp\left[i(\mathbf{k}_I \cdot \mathbf{R}_{lb} - \omega t)\right] \\ &\quad + \sum_{R_j} A_{R_j} \xi_{R_j,b\alpha} \exp[i(\mathbf{k}_{R_j} \cdot \mathbf{R}_{lb} - \omega t)] \\ u_{\mathrm{C},lb\alpha}(t) &= U_\alpha(\mathbf{R}_{lb}) \exp\left(-i\omega t\right) \\ u_{\mathrm{R},lb\alpha}(t) &= \sum_{T_p} A_{T_p} \xi_{T_p,b\alpha} \exp[i(\mathbf{k}_{T_p} \cdot \mathbf{R}_{lb} - \omega t)], \end{aligned} \tag{5}$$

where A_{R_j}, A_{T_p}, and $U_\alpha(\mathbf{R}_{lb})$ are the unknowns. The central-region atomic displacements $\mathbf{U}(\mathbf{R}_{lb})$ embody a characteristic vibrational mode, which is formed by the superposition of multiple reflected and transmitted phonons generated by the interfaces of the SL with time fixed at $t = 0$. From the central-region atomic displacements, we can extract the displacements of n atoms we are interested in, and concatenate them to form a displacement vector of dimension $3n$. In this study, we choose the nitrogen atoms in one specific atomic chain to constitute the atomic displacement vector, as elaborated in the subsequent chapter. The displacement vector will be further utilized in quantifying the phonon coherence.

The subsequent move is to assemble a large system of linear equations that includes the aforementioned unknowns. For the transmitted and reflected phonon modes, we can calculate their group velocities by taking the gradient of the frequency with respect to the wave vector. Furthermore, we can express the transmittance and reflectance of an incident phonon in terms of the group velocities in the z-direction and the amplitudes of the related phonon modes as

$$\mathcal{T} = \sum_{T_k} \frac{v_{T_p,z}}{v_{I,z}} |A_{T_p}|^2$$
$$\mathcal{R} = \sum_{R_j} \frac{|v_{R_j,z}|}{v_{I,z}} |A_{R_j}|^2. \tag{6}$$

Then we establish the following constraints: (1) The atomic displacements in the central region should satisfy Eq. (1); (2) the displacements of the atoms in the central region should be continuous with that of the atoms in the left and right regions at the boundaries; and (3) the transmittance plus the reflectance should be equal to 1. From the above constraints, a linear equation system is ultimately obtained.

The last step is to solve the equations to get the final outputs. We sample the wave vector of the incident phonon in the first Brillouin zone of AlN using the Monkhorst-Pack method [60]. For every single incident mode with wave vector k and band index s, we compute the reflected and transmitted modes, then the amplitude $A_{R_j,s}$, $A_{T_p,s}$ and the transmittance $\mathcal{T}_s$. The thermal conductance (TC) of the system can be subsequently determined by summing up the contributions from all phonon modes [61,62],

$$K = \frac{1}{V_1} \sum_{\mathbf{k},s} \hbar\omega_s(\mathbf{k}) v_{z,s}(\mathbf{k}) \mathcal{T}_s(\mathbf{k}) \frac{\partial f}{\partial T}, \tag{7}$$

where V_1 is the volume of the crystal's primitive cell, $\hbar$ is the reduced Planck constant, f is the Bose-Einstein distribution function, and T is the temperature of the system. In the following text, we calculate the TC rather than the thermal conductivity κ of the SLs; the latter can be obtained by multiplying the former by the length of the system. We simultaneously obtain the atomic displacements in the SL for further analysis.

D. Coherence analysis framework

For each phonon mode, we can extract two key features from the atomic displacement vector. The first feature is used to characterize the degree of phonon localization. We may adopt the phonon participation ratio (PR), which is defined as [63,64]

$$P = \left(\sum_{b=1}^{n} |\mathbf{U}(z_b)|^2 \right)^2 \Big/ \left(n \sum_{b=1}^{n} |\mathbf{U}(z_b)|^4 \right), \tag{8}$$

for a displacement vector $\{\mathbf{U}(z_b)\}_{b=1}^n$. A larger PR value corresponds to a more extended mode. Apart from that, we propose another localization indicator that we find more suitable for this issue, as we will show in the following chapter. We name it the center of energy in real space, which is defined as the weighted average of atomic positions, with the weights being the squared magnitudes of the displacements:

$$\mu_z = \sum_{b=1}^{n} (z_b |\mathbf{U}(z_b)|^2) / \sum_{b=1}^{n} |\mathbf{U}(z_b)|^2. \tag{9}$$

In contrast to PR, μ_z accurately characterizes the average layer to which phonon-induced atomic vibrations propagate within the SL. As we will demonstrate later, a more extended mode (which is often more coherent) has a μ_z value closer to zero, while a more localized mode has a μ_z value closer to the location of the left boundary.

The next feature is for determining the irregularity of the displacement vector, which more directly distinguishes incoherent modes from coherent modes. Here, we explain the fundamental idea behind it. In a superlattice, a coherent phonon mode is typically an extended Bloch wave, which is a plane wave modulated by a periodic amplitude [65]. In contrast, if the phonon undergoes a series of diffuse scatterings in the SL, the polar angle and z-component of the wave vector of the reflected phonons will exhibit strong randomness, causing the superposed atomic displacements to be irregular. Following this line of reasoning, we find that the quantification of irregularity can be achieved by transforming the displacement vector to wave vector space (k-space) and analyzing its energy distribution characteristics. It is worth noting that our coherence analysis framework is applicable as long as the structure is not severely amorphous, where anharmonic effects are significant, and wave vectors are no longer well defined. In other words, our method can be applied to analyze SLs with rough or even slightly amorphous interfaces.

Specifically, we first determine the principal vibration direction of the incident phonon mode by comparing the squared magnitudes of its eigenvector projections along the x, y, and z axes. After determining the principal direction (denoted by α), a preprocessing technique is required adjust the amplitude of the displacement vector so that it exhibits no significant decay with spatial position, which will be elaborated on in the next section. Then, we perform a discrete Fourier transform on the $\alpha-$ component of the displacement vector $\{U_\alpha(z_b)\}_{b=1}^n$ and obtain the amplitude spectrum in k-space $\{\tilde{U}_\alpha(k_b)\}_{b=1}^n$. Subsequently, we calculate the energy spectral density (ESD) [66] as $E_k(k_b) = |\tilde{U}_\alpha(k_b)|^2$. Finally, we propose the CDE in k-space as an indicator of phonon coherence, defined as

$$C_{E,k} = 1 - \sum_{b=1}^{n} |E_k(k_b)| \Big/ \left(n \sum_{b=1}^{n} |E_k(k_b)|^2 \right)^{1/2}. \tag{10}$$

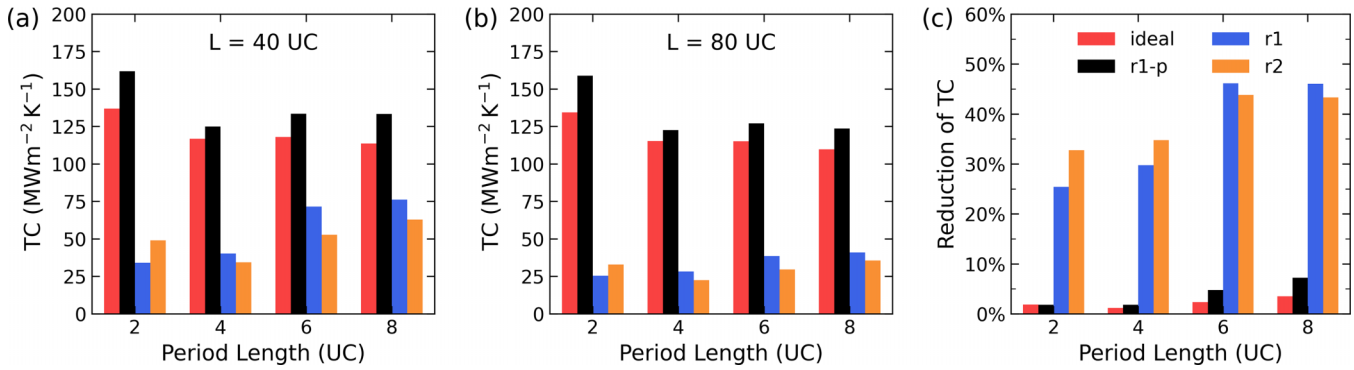

FIG. 2. (a) TC of SLs with different periodic lengths and interface structures, with a total length of 40 UC. (b) TC of SLs with different periodic lengths and interface structures, with a total length of 80 UC. (c) The reduction rate of TC after doubling the total length.

The definition of CDE in k-space incorporates the following considerations: The ratio between the l_1 norm and l_2 norm is a commonly used measure of vector sparsity [67], with $n^{1/2}$ serving as a normalization factor to ensure this term falls within the range (0, 1). As we will demonstrate later, the higher the coherence of the phonon mode, the sparser its energy distribution in k-space becomes, which results in a smaller value of the latter term of CDE, i.e., a larger CDE value.

III. RESULTS AND DISCUSSION

A. Effects of interfacial roughness on thermal conductance

We first calculate the TC of the SL structures mentioned above, with the temperature fixed to 300 K. Figures 2(a) and 2(b) show the TC of SLs with various periodic lengths and interface structures, with a total length of 40 UC and 80 UC, respectively. Within the range of 2 to 8 UC, the TC of ideal SLs decreases with the period length, with the maximum occurring at 2 UC, which is consistent with the general trend in previous studies [13,15,27]. The r1-p SLs also have the highest TC at 2 UC. For the case of r1 SLs, TC increases monotonously with period length, which is considered evidence of the dominance of incoherent phonons [13]. The trend of r2 SLs is similar to that of r1 SLs in the range of 4 to 8 UC, however, the case of 2 UC (which is equivalent to a random AlGaN alloy) does not achieve the lowest TC. Several SL structures have a TC even lower than the alloy, indicating there is a joint effect of the coherent and incoherent phonons that severely deteriorates the thermal transport [27].

At a fixed periodic length, the TC shows the following size relationship: r1-p > ideal > r1 > r2, except for the alloy. This phenomenon confirms that the interfacial roughness can lead to a higher TC than the ideal SL, as long as the periodicity is maintained. We reexamine the SL models established in previous studies [26,27,29,31] and find that the conclusion that interfacial roughness can both enhance and reduce the TC can be unified by whether the periodicity is maintained or not.

We further obtain the rate of reduction in TC when the total length of the SL is doubled [Fig. 2(c)]. If periodicity is maintained, the TC does not decrease by more than 10%, which means the newly introduced multiple interfaces have a very limited influence on the overall thermal resistance, further corroborating the fact that phonons dominating heat transfer are the selected coherent superlattice modes. As a contrast, the TC of SLs with disrupted periodicity decreases by 25% to 50%, implying the increase of incoherent scatterings at the interfaces. These findings indicate that maintaining periodicity is crucial for ensuring the total thermal resistance of the SL remains stable at a low value and is virtually insensitive to variations in the number of periods, which can serve as guidance for the fabrication of SLs in real devices.

To gain an insight into the thermal transport in these structures, we conduct a mode-resolved analysis on phonon transmittance and thermal conductance. We take r1-p and r1 SLs for comparison, with a total length of 80 UC and a period length of 4 UC as a typical case. We first plot the Brillouin zone of bulk AlN in Fig. 3(a), where Γ-M-K-Γ-A-L-H-Γ-L is chosen as a high-symmetry path for subsequent calculations. We then calculate the spectral TC based on each phonon mode's contribution to the total TC, as shown in Fig. 3(b). The main contributions to the TC of both the r1-p SL and the r1 SL come from low-frequency phonons below 10 THz, while the major difference in their TC originates from the contributions of phonons in the range of 2 to 10 THz.

Subsequently, we calculate the phonon dispersion relation of bulk AlN with the mode-resolved transmittance along the high-symmetry path. The results of r1-p and r1 are shown in Figs. 3(c) and 3(d), respectively. Phonon modes with high transmittance are mainly distributed in the first three branches (acoustic phonon branches) and in the frequency range below 10 THz, which is in accordance with the results of spectral TC. In the high-frequency path A-L-H and the path Γ-M-K-Γ, phonons can hardly pass through. We denote the three acoustic phonon branches as TA1, TA2, and LA, where for the same wave vector, their frequencies follow the order TA1 < TA2 < LA. We further conduct the same calculations on the ideal and r2 SLs, and confirm that the differences in phonon transmittance of these SLs are most pronounced in acoustic branches along the Γ-A, Γ-L, and Γ-H paths. Therefore, the subsequent research is conducted over the acoustic phonons in the ΓAL and ΓAH regions.

B. Characteristics of atomic displacements

In the remainder of this article, we focus on the four types of SLs with the total length fixed at 80 UC and the period length fixed at 4 UC. To gain an in-depth and intuitive un-

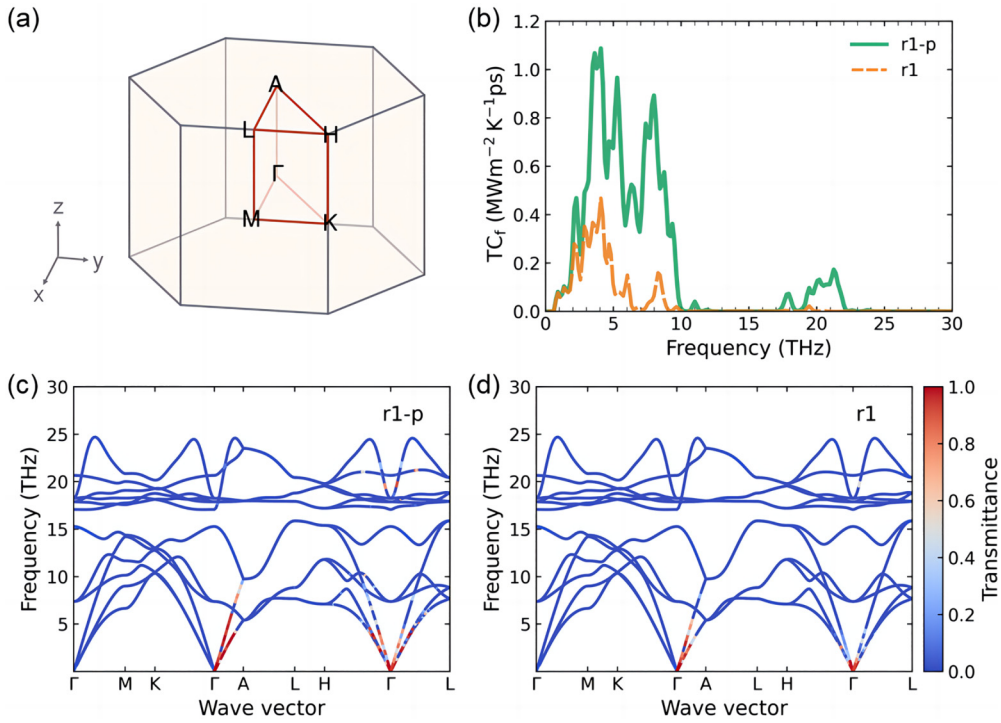

FIG. 3. (a) The Brillouin zone of bulk AlN with special k-points. (b) The spectral TC of r1-p and r1 SLs. (c) The transmittance of phonons along the high-symmetry path of r1-p SL. (d) The transmittance of phonons along the high-symmetry path of r1 SL.

derstanding of phonon transport, we need to investigate the atomic displacements induced by different phonon modes. We start by examining the phonon transmission spectra of the three acoustic phonons along the Γ-A path in the Brillouin zone, as shown in Fig. 4. We find that the transmission spectra of the LA phonons of ideal and r1-p SLs exhibit a characteristic of alternating high-transmittance and low-transmittance regions, which is a typical result of coherent transport [16,68]. For r1 and r2 SLs, the transmission spectra of the LA phonons also have the stop band structure below 5 THz. However, there are few modes that achieve high transmittance above 5 THz, especially for the r2 SL, indicating that the diffuse scattering at the interfaces together with the aperiodicity deteriorates the coherence of phonon transport.

In the cases of TA phonons, the transmission spectra of the ideal SL have four stop bands between the high-transmittance regions below 4 THz, while the transmittance drops to zero above 4 THz. We calculate the transmission spectra of the TA phonons across a single GaN/AlN interface, and find that the transmittance decreases with the increase of frequency, dropping to zero precisely at 4 THz. This phenomenon is caused by the absence of phonon modes in bulk GaN that can match the incident phonon mode from AlN. Hence, the high-frequency phonons with zero transmittance in the ideal SL have a transport mechanism that is different from both coherent and incoherent transport, but the same as the evanescent modes in a single-interface system. We propose a new terminology, 'nonpropagating modes', as the third category of phonon modes in superlattice systems, alongside the coherent and incoherent modes. For the r1-p SLs, several frequency ranges above 4 THz still exhibit high transmittance. This can be explained as the interfacial roughness reduces the mismatch of the two materials [29,30]. The enhancement of transmittance at the stop bands, as well as the high-frequency range, can explain the fact that the r1-p SL have a TC higher than the ideal SL. As for r1 and r2 SLs, the transmittance of a few phonons above 4 THz also shows an increase compared to the ideal SL, but it remains at a low level. We infer that these phonons have weak coherence, although they successfully pass through the SL.

We then select six representative phonon modes according to Fig. 4 and calculate the corresponding atomic displacements in the SLs. Among these modes, three are typical coherent modes (labeled as C1, C2, and C3), with the first two selected from the LA branch of the ideal SL, and the other being the high-frequency, high-transmittance TA2 phonon of the r1-p SL. TA2 phonon of ideal SL that share the same frequency with C3 is selected as a typical nonpropagating mode, labeled as N. There are also two typical incoherent modes, one is the high-frequency TA1 phonon of r1 SL, which have a transmittance slightly higher than zero (so that it cannot be the nonpropagating mode, labeled as I1), the other is the high-frequency LA phonon of r2 SL (labeled as I2). The size of our SL models in the xy-plane is 2 UC × 2 UC, thus it can be considered as composed of four parallel atomic chains along the z-direction, with atoms in each chain sharing the same x and y coordinates. To simplify the calculation while retaining the key features, we select one specific atomic chain and calculate only the displacements of the nitrogen atoms to form the displacement vector.

We present the atomic displacements of the above phonon modes in Fig. 5. Specifically, we plot the three components of the real part of atomic displacements in Cartesian coordinates at a fixed time of $t = 0$, and the two vertical dashed lines in

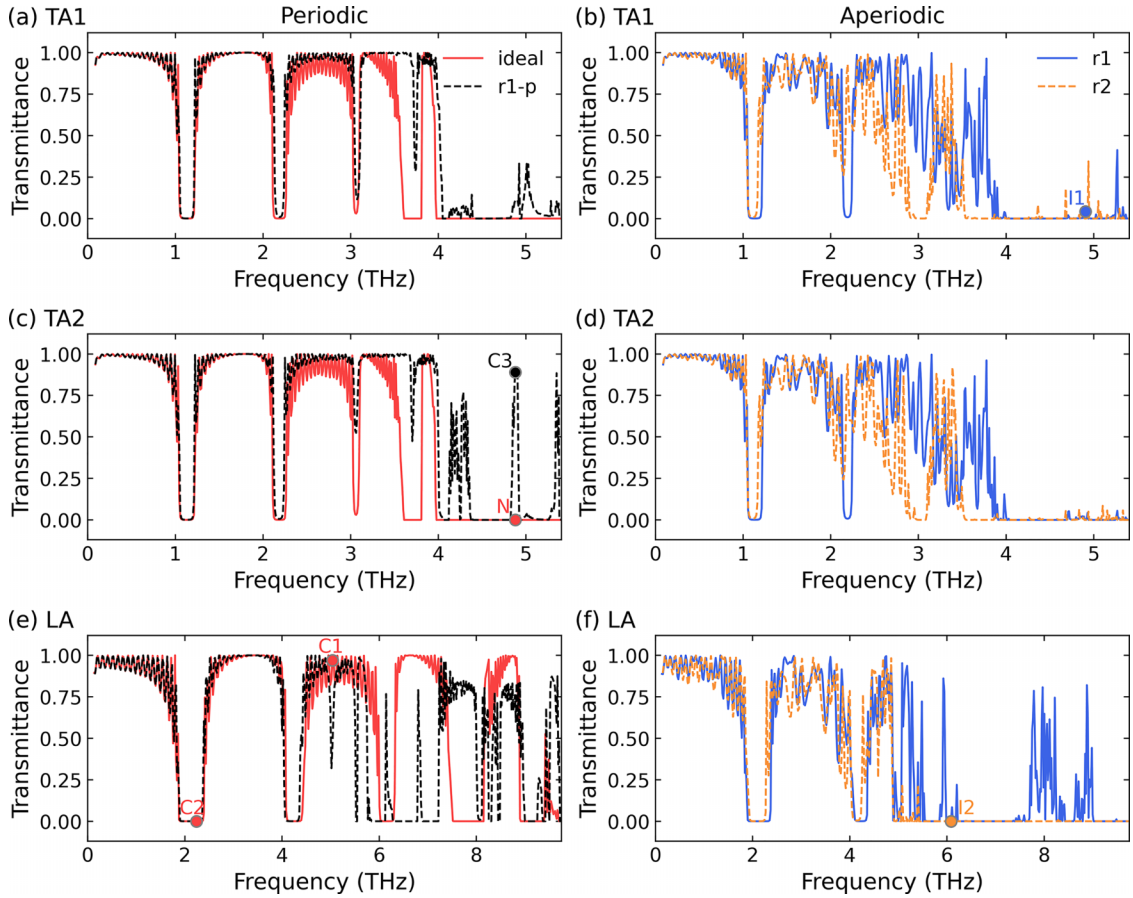

FIG. 4. Transmission spectra of vertically incident (a) TA1 phonons in periodic SLs, (b) TA1 phonons in aperiodic SLs, (c) TA2 phonons in periodic SLs, (d) TA2 phonons in aperiodic SLs, (e) LA phonons in periodic SLs, and (f) LA phonons in aperiodic SLs. Six special points used for atomic displacement analysis are marked with circles.

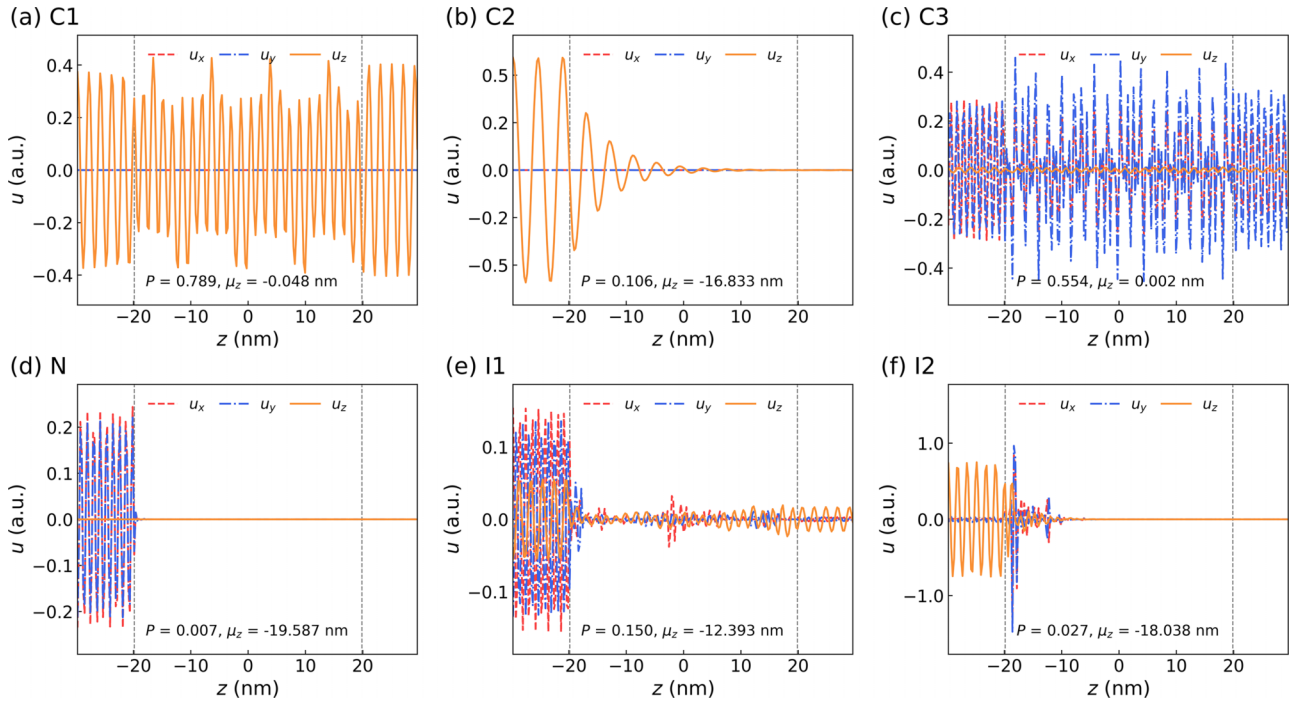

FIG. 5. Atomic displacements of the six representative phonon modes with calculated μ_z and PR, where the dashed lines denote the left and right boundaries of the SLs. (a) Coherent mode 1. (b) Coherent mode 2. (c) Coherent mode 3. (d) Nonpropagating mode. (e) Incoherent mode 1. (f) Incoherent mode 2.

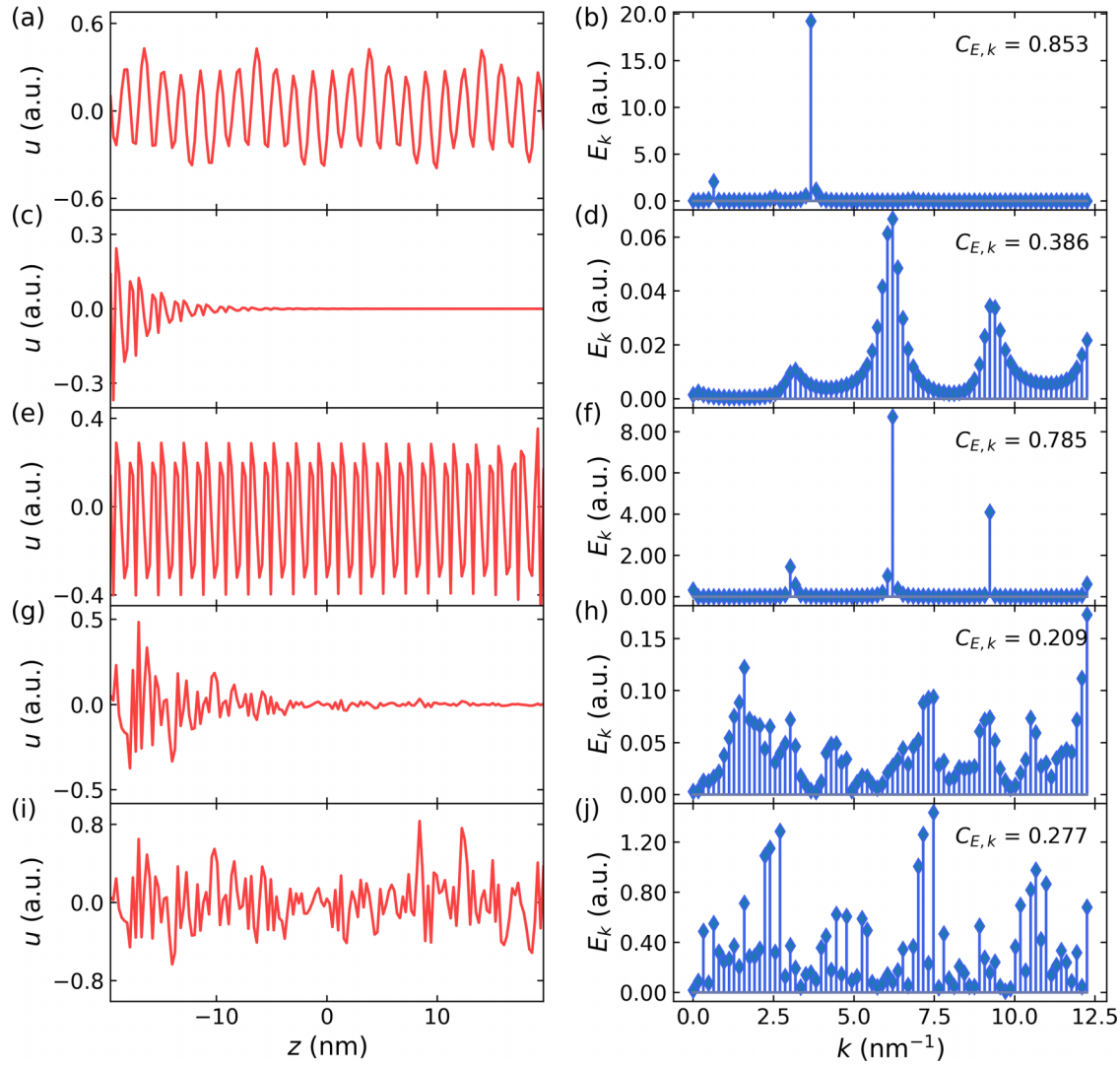

FIG. 6. Atomic displacement vectors (real part only, in the principal vibration direction) and their corresponding ESD. (a), (b) Nonlocalized coherent mode. (c), (d) Localized coherent mode. (e), (f) Localized coherent mode after amplitude recovery. (g), (h) Incoherent mode. (i), (j) Incoherent mode after amplitude recovery.

each figure denote the left and right boundaries of the SLs. We can observe that the x- and y-components of the atomic displacements for C1 and C2 are both zero, which is consistent with the fact that they are LA phonons. The atomic displacements of C1, C2, and C3 all conform to the characteristics of coherent transport. C1 and C3 are typical Bloch waves, which are plane waves modulated by periodic amplitudes. C2 is a localized wave resulting from Bragg reflection, a plane wave enveloped by an exponentially decaying amplitude [16].

Among the other three modes, N and I2 are also localized, yet different from C2. After entering the left interface of the SL, the amplitude of the atomic displacements in the N-mode shows a steep drop to zero. For the cases of I1 and I2, the atomic displacements exhibit an irregular pattern, owing to the randomization of the z-component of the wave vector of the reflected phonons caused by interfacial diffuse scatterings. Apart from the above findings, we notice the mode-conversion effects in I1 and I2. Since these two modes are vertically incident TA modes, the z-components of their atomic displacements should equal zero, yet results show that there are z-direction vibrations inside and outside the SLs, indicating that the LA mode has been excited during the interface scattering process. While the mode-conversion phenomenon has been demonstrated theoretically and computationally [69,70], our study offers an intuitive picture of this physical process.

Our next move is to validate the effectiveness of the proposed coherence analysis framework by calculating the features of atomic displacements. First, we compute the PR and center of energy in real space (μ_z) to reveal the degree of localization of the phonon modes. From now on, we only select atoms within the SLs (the region between the dashed lines in Fig. 5) to form the displacement vector $\{\mathbf{U}(z_b)\}_{b=1}^{n}$. As shown in Fig. 5, the nonlocalized modes C1 and C3 have large PR values and near-zero values of μ_z. The more severe the localization, the closer the value of PR is to $1/n$, and the closer the value of μ_z is to -19.88 nm (the location of the left boundary of the SL). We consider phonon modes

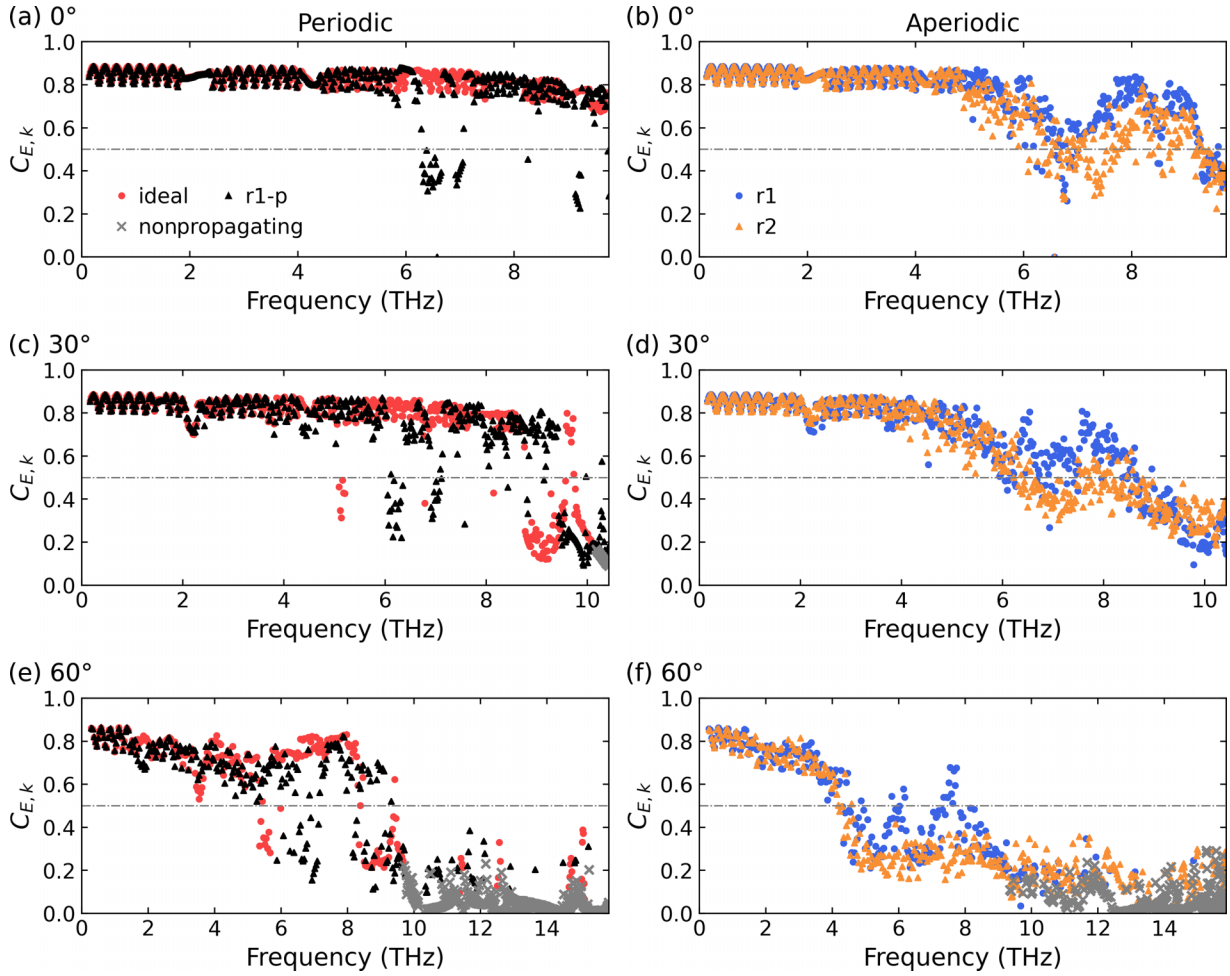

FIG. 7. CDE as a function of frequency for LA phonons with incident angle of (a), (b) 0°, (c), (d) 30°, and (e), (f) 60°. The gray 'x' markers denote the nonpropagating modes. The horizontal dot-dash lines mark the position where $C_{E,k} = 0.5$.

with μ_z smaller than the z-coordinate of the center of the left-most GaN layer (−19.35 nm in this case) are nonpropagating, because phonon modes with larger μ_z values are considered capable of passing through at least one GaN layer.

After quantitatively distinguishing between nonpropagating and propagating modes, we subsequently test the performance of CDE in k-space in quantitatively differentiating coherent and incoherent modes among the propagating modes. Figure 6 shows the atomic displacement vectors (real part only, in the principal vibration direction) and the ESD for three representative phonon modes: nonlocalized coherent, localized coherent, and incoherent. The latter two modes are further used to illustrate the preprocessing technique of the displacement vector and its effectiveness.

For a nonlocalized coherent mode [Fig. 6(a)], the ESD exhibits only two major peaks that correspond to the inherent and Bloch periodicities, respectively [Fig. 6(b)]. The calculated CDE is greater than 0.8, which is a large value. For a localized coherent mode which is nonperiodic [Fig. 6(c)], the ESD obtained directly from the Fourier transform is dense, resulting in a small CDE value. Now, we construct an envelope for the displacement vector, fit the envelope with the exponential function exp(-az) to obtain the parameter a, and then multiply the displacement vector by exp(az) to achieve amplitude recovery [Fig. 6(e)]. It can be observed that the recovered displacement vector exhibits a high degree of periodicity, the corresponding ESD becomes sparse, and the CDE value also shows significant improvement. In Figa. 6(g)–6(j), we verify that incoherent modes, which also feature decaying amplitudes, do not achieve high CDE values even after amplitude recovery. It can be observed that the displacement vector remains irregular in Fig. 6(i), corresponding to a dense ESD in Fig. 6(j) and a CDE value less than 0.3. Moreover, further testing reveals that amplitude recovery does not negatively affect the case shown in Fig. 6(a), since the fitted parameter a in this scenario is close to zero and thus exp(-az) has little influence on the amplitude. The above results conclusively demonstrate the efficacy of the CDE in k-space in quantifying phonon coherence.

C. Statistical analysis on phonon coherence

Since μ_z and CDE in k-space have demonstrated good performance in quantifying localization and coherence, respectively, we apply them to conduct a statistical analysis of phonon modes in the four types of SLs, aiming to reveal in detail the influence of frequency, incident angle, and interface structure on phonon transport. We uniformly sample the wave

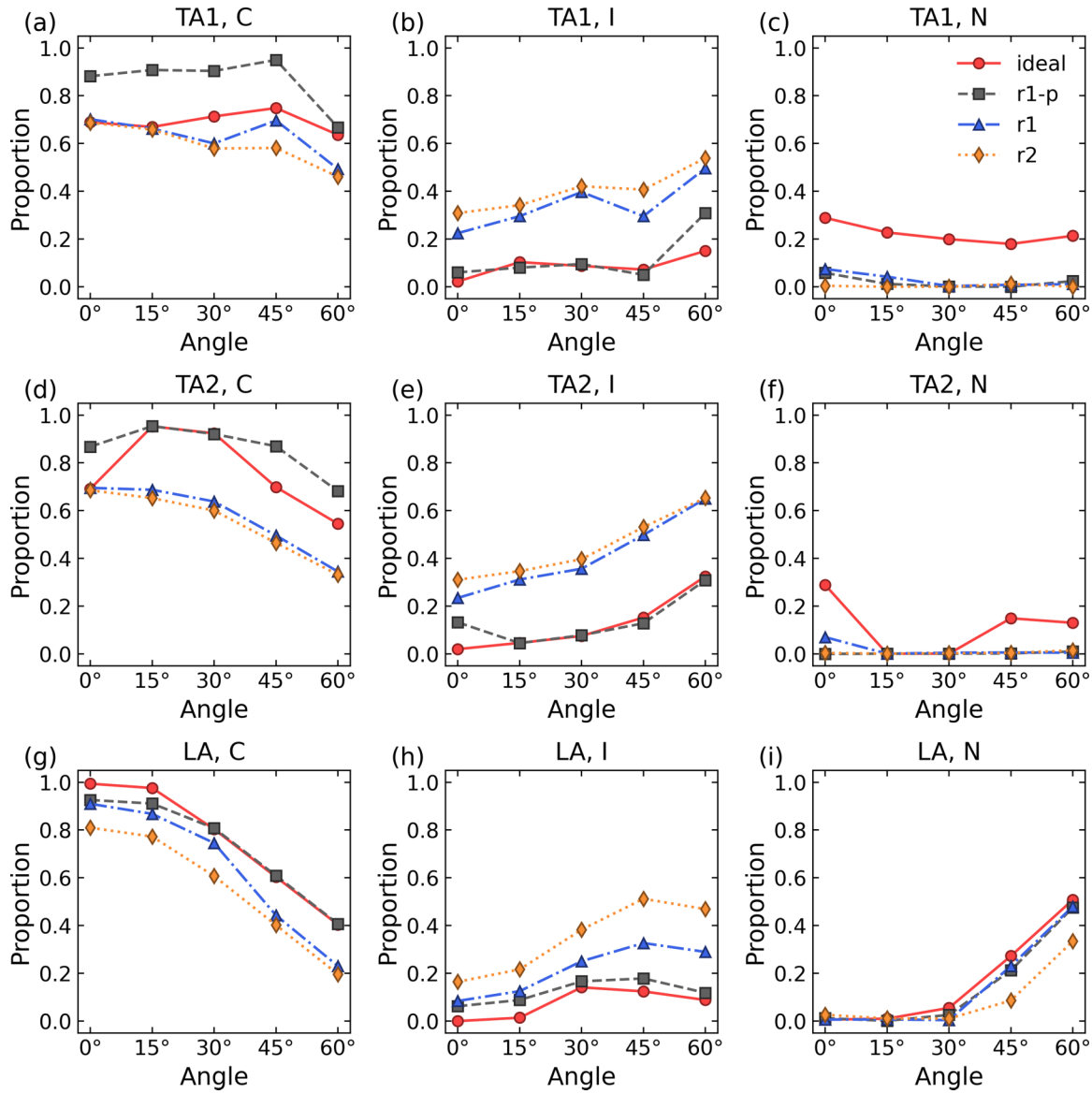

FIG. 8. Proportion of coherent (C), incoherent (I), and nonpropagating (N) modes at every incident angle for (a)–(c) TA1, (d)–(f) TA2, and (g)–(i) LA phonons in the four types of SLs.

vectors of acoustic phonons along the 0°, 15°, 30°, 45°, and 60° directions in the ΓAL region of the Brillouin zone and subsequently compute μ_z and CDE of these modes. Figure 7 shows the CDE as a function of frequency for LA phonons with different incident angles, where the gray 'x' markers denote the nonpropagating modes with μ_z less than the threshold value we set. We find that in the case where the incident angle equals 0°, the CDE of phonons in the ideal SL is above 0.5 across the entire frequency range, although it shows a slight decrease with increasing frequency. As a comparison, the CDE of a few phonon modes in the r1-p SL is below 0.5. For r1 and r2 SLs, the CDE begins to decrease at 5 THz, recovers at around 7 THz, and then shows a downward trend again after 8 THz. Overall, the CDE of the r1 SL is higher than that of the r2 SL.

As the incident angle becomes larger, the ideal SL also have phonon modes with CDE below 0.5, especially in the high-frequency region. For r1 and r2 SLs, the recover-after-decrease effect becomes less obvious, and the decrease of CDE happens at a lower frequency. We notice that for the r2 SL, the CDE has a clear critical frequency of about 4.5 THz. The related phonon wavelength of this frequency is 2.27 nm, which is approximately 4 times the interfacial roughness. This suggests that the destructive effect of interfacial roughness on phonon coherence is more severe than previously understood [36,48]. As we can see, increased interfacial roughness, frequency, and incident angle all lead to a reduction in phonon coherence, though not in a simple linear relationship. The nonpropagating modes are dispersed in the region above 9 THz, and the CDE values of these modes are also very low. To demonstrate the scalability of our coherence analysis framework, we further applied it to SL structures with poorer periodicity (see Supplemental Material, Note C [53]).

From the results in Fig. 7, there is no clear boundary between coherent and incoherent modes. Nevertheless, after further statistics, we find that the CDE values of all sampled

phonons exhibit a distinct bimodal distribution, indicating the clusters of coherent and incoherent modes (see Supplemental Material, Fig. S5 [53]). The valley between the two clusters is centered approximately at 0.5, thus we choose CDE equals 0.5 as the threshold to distinguish between coherent and incoherent modes. Based on this criterion, we statistically analyze the proportion of coherent, incoherent, and nonpropagating modes at every incident angle for each acoustic branch in the four types of SLs, with the results shown in Fig. 8. We first examine the LA phonons. Interestingly, all four SLs follow the following patterns: as the incident angle increases, the proportion of coherent modes decreases monotonously, the proportion of incoherent modes first increases and then decreases, and the proportion of nonpropagating modes increases monotonously. It can be clearly observed that as the angle increases, a large number of phonon modes undergo a transition from coherent to incoherent or nonpropagating: at an incident angle of 0°, the lowest proportion of coherent modes among the four SLs exceeds 0.8, while at an incident angle of 60°, the highest proportion of coherent modes among the four SLs is only around 0.4. For the same angle, the proportion of coherent modes follows the relationship ideal $\geqslant$ r1-p $>$ r1 $>$ r2, the proportion of incoherent modes follows the relationship ideal $<$ r1-p $<$ r1 $<$ r2, and the proportion of nonpropagating modes follows the relationship ideal $>$ r1-p $\approx$ r1 $>$ r2.

For TA1 and TA2 phonons, the situation becomes more complex, but the following patterns can still be summarized. In r1 and r2 SLs, the proportion of coherent modes generally decreases with increasing incident angle, while the proportion of incoherent modes generally increases with the incident angle. At a fixed incident angle, r1 and r2 SLs still exhibit significantly lower coherent mode proportions and significantly higher incoherent mode proportions compared to the other two SLs. It is intriguing that the r1-p SL has a higher proportion of coherent modes than the ideal SL, which differs from the LA phonon case, yet the ideal SL shows a slightly smaller or nearly equal proportion of incoherent modes. The lower coherent mode proportion in the ideal SL is actually due to its higher proportion of nonpropagating modes rather than incoherent modes, and the nonpropagating effect of phonons in the ideal SL is remarkably stronger compared to the other SLs. This detailed insight is attributed to our framework that comprehensively incorporates coherent, incoherent, and nonpropagating phonon modes. We can now conclusively explain the superior thermal conductivity of r1-p SLs over ideal SLs: maintaining SL periodicity reduces incoherent phonon modes, while increased interfacial roughness suppresses nonpropagating modes. The synergy of these two effects enables a significant proportion of phonons to traverse the superlattice coherently, leading to superior thermal transport. Moreover, we perform sensitivity testing on the threshold CDE = 0.5 by adjusting it to 0.4 and 0.6, respectively, and recalculated the proportions of the three phonon modes in each case (see Supplemental Material, Figs. S6 and S7 [53]). Our findings indicate that neither of these alternative threshold settings alters the aforementioned trends or the final conclusions.

IV. CONCLUSION

In summary, we have developed a phonon coherence analysis framework based on LD with a MACE potential, introducing two quantitative metrics—μ_z to characterize localization and CDE in k-space to measure coherence. By applying this framework to GaN/AlN SLs, we confirm that interfacial roughness can enhance thermal conductivity and clarify that the critical condition for this phenomenon is that the inherent periodicity of the superlattice must be preserved. Our analysis further elucidates that the underlying mechanism is that the increase in interfacial roughness simultaneously introduces more incoherent modes and enables more modes to propagate. Crucially, we demonstrate that maintaining periodicity is the key factor that significantly enhances phonon coherence. This finding provides a direct explanation for why SLs with moderate, periodicity-preserving roughness can achieve superior phonon coherence and higher thermal conductivity compared to ideal structures. The proposed coherence analysis framework is broadly applicable to general SL systems, offering quantitative guidance for tailoring thermal conductivity through interfacial roughness engineering.

ACKNOWLEDGMENTS

This study was financially supported by the National Natural Science Foundation of China (NSFC) (Grants No. 52425601, No. 52327809, and No. 52250273), the Beijing Natural Science Foundation (Grant No. L233022), and the National Key Research and Development Program of China (Grant No. 2023YFB4404104).

DATA AVAILABILITY

The data that support the findings of this article are openly available [71].

[1] U. K. Mishra, S. Likun, T. E. Kazior, and Y.-F. Wu, GaN-based RF power devices and amplifiers, Proc. IEEE **96**, 287 (2008).

[2] S. Li, P. Sun, Z. Xing, N. Wu, W. Wang, and G. Li, Degradation mechanisms of Mg-doped GaN/AlN superlattices HEMTs under electrical stress, Appl. Phys. Lett. **121**, 062101 (2022).

[3] T. Ueda, M. Ishida, T. Tanaka, and D. Ueda, GaN transistors on Si for switching and high-frequency applications, Jpn. J. Appl. Phys. **53**, 100214 (2014).

[4] K. Yuk, G. R. Branner, and C. Cui, Future directions for GaN in 5G and satellite communications, in *2017 IEEE 60th International Midwest Symposium on Circuits and Systems (MWSCAS)* (IEEE, Boston, MA, USA, 2017), pp. 803–806.

[5] N. Islam, M. F. P. Mohamed, M. F. A. J. Khan, S. Falina, H. Kawarada, and M. Syamsul, Reliability, applications and challenges of GaN HEMT technology for modern power devices: A review, Crystals **12**, 1581 (2022).

[6] L. Esaki and R. Tsu, Superlattice and negative differential conductivity in semiconductors, IBM J. Res. & Dev. **14**, 61 (1970).

[7] M. Xiao, W. Zhang, Y. Zhang, H. Zhou, K. Dang, J. Zhang, and Y. Hao, Novel 2000 V normally-off MOS-HEMTs

using AlN/GaN superlattice channel, in *2019 31st International Symposium on Power Semiconductor Devices and ICs (ISPSD)* (IEEE, Shanghai, China, 2019), pp. 471–474.

[8] P. Dalapati, S. Urata, and T. Egawa, Investigation of AlGaN/GaN high electron mobility transistors on Silicon (111) substrates employing multi-stacked strained layer superlattice structures, Superlattices Microstruct. **147**, 106709 (2020).

[9] L. T. Hieu, H.-T. Hsu, C.-H. Chiang, D. Panda, C.-T. Lee, C.-H. Lin, and E. Y. Chang, Effects of AlN/GaN superlattice buffer layer on performances of AlGaN/GaN HEMT grown on silicon for sub-6 GHz applications, Semicond. Sci. Technol. **38**, 025006 (2023).

[10] Z.-L. Tang, Y. Shen, and B.-Y. Cao, Modulating self-heating effects in GaN HEMTs using slant field plate, IEEE Trans. Electron Devices **72**, 1907 (2025).

[11] Y. Shen, H.-A. Yang, and B.-Y. Cao, Near-junction phonon thermal spreading in GaN HEMTs: A comparative study of simulation techniques by full-band phonon Monte Carlo method, Int. J. Heat Mass Transfer **211**, 124284 (2023).

[12] B. Padmanabhan, D. Vasileska, and S. M. Goodnick, Reliability concerns due to self-heating effects in GaN HEMTs, JICS **8**, 78 (2020).

[13] J. Ravichandran, *et al.*, Crossover from incoherent to coherent phonon scattering in epitaxial oxide superlattices, Nat. Mater **13**, 168 (2014).

[14] M. N. Luckyanova, *et al.*, Coherent phonon heat conduction in superlattices, Science **338**, 936 (2012).

[15] J. Garg, N. Bonini, and N. Marzari, High thermal conductivity in short-period superlattices, Nano Lett. **11**, 5135 (2011).

[16] S. Tamura, D. C. Hurley, and J. P. Wolfe, Acoustic-phonon propagation in superlattices, Phys. Rev. B **38**, 1427 (1988).

[17] A. H. Nayfeh, *Wave Propagation in Layered Anisotropic Media: With Applications to Composites* (Elsevier, Amsterdam, New York, 1995).

[18] B. Yang and G. Chen, Partially coherent phonon heat conduction in superlattices, Phys. Rev. B **67**, 195311 (2003).

[19] G. Xie, D. Ding, and G. Zhang, Phonon coherence and its effect on thermal conductivity of nanostructures, Adv. Physics: X **3**, 1480417 (2018).

[20] Y. Ni and S. Volz, Evidence of phonon Anderson localization on the thermal properties of disordered atomic systems, J. Appl. Phys. **130**, 190901 (2021).

[21] G. Chen and M. Neagu, Thermal conductivity and heat transfer in superlattices, Appl. Phys. Lett. **71**, 2761 (1997).

[22] S. Hu, H. Zhang, S. Xiong, H. Zhang, H. Wang, Y. Chen, S. Volz, and Y. Ni, Screw dislocation induced phonon transport suppression in SiGe superlattices, Phys. Rev. B **100**, 075432 (2019).

[23] Y. Wang, H. Huang, and X. Ruan, Decomposition of coherent and incoherent phonon conduction in superlattices and random multilayers, Phys. Rev. B **90**, 165406 (2014).

[24] T. Juntunen, O. Vänskä, and I. Tittonen, Anderson localization quenches thermal transport in aperiodic superlattices, Phys. Rev. Lett. **122**, 105901 (2019).

[25] R. Hu, S. Iwamoto, L. Feng, S. Ju, S. Hu, M. Ohnishi, N. Nagai, K. Hirakawa, and J. Shiomi, Machine-learning-optimized aperiodic superlattice minimizes coherent phonon heat conduction, Phys. Rev. X **10**, 021050 (2020).

[26] S. C. Huberman, J. M. Larkin, A. J. H. McGaughey, and C. H. Amon, Disruption of superlattice phonons by interfacial mixing, Phys. Rev. B **88**, 155311 (2013).

[27] Y. Wang, C. Gu, and X. Ruan, Optimization of the random multilayer structure to break the random-alloy limit of thermal conductivity, Appl. Phys. Lett. **106**, 073104 (2015).

[28] A. Malhotra, K. Kothari, and M. Maldovan, Cross-plane thermal conduction in superlattices: Impact of multiple length scales on phonon transport, J. Appl. Phys. **125**, 044304 (2019).

[29] Z. Tian, K. Esfarjani, and G. Chen, Green's function studies of phonon transport across Si/Ge superlattices, Phys. Rev. B **89**, 235307 (2014).

[30] Z. Tian, K. Esfarjani, and G. Chen, Enhancing phonon transmission across a Si/Ge interface by atomic roughness: First-principles study with the Green's function method, Phys. Rev. B **86**, 235304 (2012).

[31] K. Termentzidis, P. Chantrenne, J.-Y. Duquesne, and A. Saci, Thermal conductivity of GaAs/AlAs superlattices and the puzzle of interfaces, J. Phys.: Condens. Matter **22**, 475001 (2010).

[32] M. V. Simkin and G. D. Mahan, Minimum thermal conductivity of superlattices, Phys. Rev. Lett. **84**, 927 (2000).

[33] D. G. Cahill, W. K. Ford, K. E. Goodson, G. D. Mahan, A. Majumdar, H. J. Maris, R. Merlin, and S. R. Phillpot, Nanoscale thermal transport, J. Appl. Phys. **93**, 793 (2003).

[34] B. Latour, S. Volz, and Y. Chalopin, Microscopic description of thermal-phonon coherence: From coherent transport to diffuse interface scattering in superlattices, Phys. Rev. B **90**, 014307 (2014).

[35] G. Chen, Non-Fourier phonon heat conduction at the microscale and nanoscale, Nat. Rev. Phys. **3**, 555 (2021).

[36] G. Chen, *Nanoscale Energy Transport and Conversion: A Parallel Treatment of Electrons, Molecules, Phonons, and Photons* (Oxford University Press, New York, NY, 2005).

[37] D. A. Young and H. J. Maris, Lattice-dynamical calculation of the Kapitza resistance between fcc lattices, Phys. Rev. B **40**, 3685 (1989).

[38] S. Tamura, Y. Tanaka, and H. J. Maris, Phonon group velocity and thermal conduction in superlattices, Phys. Rev. B **60**, 2627 (1999).

[39] H. Zhao and J. B. Freund, Lattice-dynamical calculation of phonon scattering at ideal Si–Ge interfaces, J. Appl. Phys. **97**, 024903 (2005).

[40] K. Gordiz and A. Henry, Phonon transport at crystalline Si/Ge interfaces: The role of interfacial modes of vibration, Sci. Rep. **6**, 23139 (2016).

[41] H.-A. Yang and B.-Y. Cao, Mode-resolved phonon transmittance using lattice dynamics: Robust algorithm and statistical characteristics, J. Appl. Phys. **134**, 155302 (2023).

[42] E. R. Hoglund, *et al.*, Nonequivalent atomic vibrations at interfaces in a polar superlattice, Adv. Mater. **36**, 2402925 (2024).

[43] P. K. Schelling, S. R. Phillpot, and P. Keblinski, Phonon wave-packet dynamics at semiconductor interfaces by molecular-dynamics simulation, Appl. Phys. Lett. **80**, 2484 (2002).

[44] L. Sun and J. Y. Murthy, Molecular dynamics simulation of phonon scattering at silicon/germanium interfaces, J. Heat Transfer **132**, 102403 (2010).

[45] P. K. Schelling, S. R. Phillpot, and P. Keblinski, Kapitza conductance and phonon scattering at grain boundaries by simulation, J. Appl. Phys. **95**, 6082 (2004).

[46] P. K. Schelling and S. R. Phillpot, Multiscale simulation of phonon transport in superlattices, J. Appl. Phys. **93**, 5377 (2003).
[47] T. Maranets and Y. Wang, How phonon coherence develops and contributes to heat conduction in periodic and aperiodic superlattices, Int. J. Therm. Sci. **217**, 110018 (2025).
[48] M. Maldovan, Phonon wave interference and thermal bandgap materials, Nat. Mater **14**, 667 (2015).
[49] A. Alkurdi, S. Pailhès, and S. Merabia, Critical angle for interfacial phonon scattering: Results from *ab initio* lattice dynamics calculations, Appl. Phys. Lett. **111**, 093101 (2017).
[50] I. Batatia, D. P. Kovács, G. N. C. Simm, C. Ortner, and G. Csányi, MACE: Higher order equivariant message passing neural networks for fast and accurate force fields, Adv. Neural Info. Proc. Syst. **35**, 11423 (2022).
[51] J. P. Freedman, J. H. Leach, E. A. Preble, Z. Sitar, R. F. Davis, and J. A. Malen, Universal phonon mean free path spectra in crystalline semiconductors at high temperature, Sci. Rep. **3**, 2963 (2013).
[52] R. L. Xu, *et al.*, Thermal conductivity of crystalline AlN and the influence of atomic-scale defects, J. Appl. Phys. **126**, 185105 (2019).
[53] See Supplemental Material at http://link.aps.org/supplemental/10.1103/q6d9-mqs6 for additional simulation details, results, and discussions.
[54] I. Batatia, *et al.*, A foundation model for atomistic materials chemistry, J. Chem. Phys. **163**, 184110 (2025).
[55] Y. Liu, H. Liang, L. Yang, G. Yang, H. Yang, S. Song, Z. Mei, G. Csányi, and B. Cao, Unraveling thermal transport correlated with atomistic structures in amorphous gallium oxide via machine learning combined with experiments, Adv. Mater. **35**, 2210873 (2023).
[56] G. Kresse and J. Hafner, *Ab initio* molecular-dynamics simulation of the liquid-metal–amorphous-semiconductor transition in germanium, Phys. Rev. B **49**, 14251 (1994).
[57] G. Kresse and D. Joubert, From ultrasoft pseudopotentials to the projector augmented-wave method, Phys. Rev. B **59**, 1758 (1999).
[58] J. P. Perdew, K. Burke, and M. Ernzerhof, Generalized gradient approximation made simple, Phys. Rev. Lett. **77**, 3865 (1996).
[59] A. Togo, First-principles phonon calculations with phonopy and phono3py, J. Phys. Soc. Jpn. **92**, 012001 (2023).
[60] H. J. Monkhorst and J. D. Pack, Special points for Brillouin-zone integrations, Phys. Rev. B **13**, 5188 (1976).
[61] J.-S. Wang, J. Wang, and J. T. Lu, Quantum thermal transport in nanostructures, Eur. Phys. J. B **62**, 381 (2008).
[62] J. Chen, X. Xu, J. Zhou, and B. Li, Interfacial thermal resistance: Past, present, and future, Rev. Mod. Phys. **94**, 025002 (2022).
[63] J. Hafner and M. Krajci, Propagating and confined vibrational excitations in quasicrystals, J. Phys.: Condens. Matter **5**, 2489 (1993).
[64] S. Pailhès, H. Euchner, V. M. Giordano, R. Debord, A. Assy, S. Gomès, A. Bosak, D. Machon, S. Paschen, and M. De Boissieu, Localization of propagative phonons in a perfectly crystalline solid, Phys. Rev. Lett. **113**, 025506 (2014).
[65] C. Kittel and P. McEuen, *Introduction to Solid State Physics* (John Wiley & Sons, Hoboken, NJ, 2018).
[66] L. Jackson, S. Kay, and N. Vankayalapati, Iterative method for nonlinear FM synthesis of radar signals, IEEE Trans. Aerosp. Electron. Syst. **46**, 910 (2010).
[67] N. Hurley and S. Rickard, Comparing measures of sparsity, IEEE Trans. Inform. Theory **55**, 4723 (2009).
[68] Y. Chen, D. Li, J. R. Lukes, Z. Ni, and M. Chen, Minimum superlattice thermal conductivity from molecular dynamics, Phys. Rev. B **72**, 174302 (2005).
[69] Hatsuyoshi Kato, H. J. Maris, and S. Tamura, Enhancement of mode-converted transmission of phonons in superlattices, Physica B **219–220**, 696 (1996).
[70] T. Yoshihiro and N. Nishiguchi, Mode-conversion effects of phonons on Anderson localization, Phys. Rev. B **100**, 235441 (2019).
[71] https://doi.org/10.5281/zenodo.17761615.